


Lubrication with Non-Newtonian Fluids

B. Veltkamp,¹ J. Jagielka,¹ K.P. Velikov,^{1,2} and Daniel Bonn^{1,*}

¹*Van der Waals-Zeeman Institute, Institute of Physics, University of Amsterdam, Science Park 904, 1098XH Amsterdam, Netherlands*

²*Unilever Innovation Centre Wageningen, Bronland 14, 6708 WH Wageningen, Netherlands*

 (Received 26 October 2021; revised 3 June 2022; accepted 15 November 2022; published 20 January 2023)

Hydrodynamic lubrication is studied for both shear thinning and viscoelastic polymer solutions. We find that elasticity, notably strong normal stresses, does not change the friction significantly for the range of parameters tested in this manuscript. Shear-thinning properties, on the other hand, do change the formation of the lubricating layer thickness and the dependence of friction on velocity relative to Newtonian fluids. A hydrodynamic model that includes shear thinning is developed and compared to experimental data. The model describes the dependence on lubrication parameters well, but underestimates the lubricating layer thickness by a constant factor of roughly 1.5. The theory allows us to define a Hersey-like number for shear-thinning fluids that describes the lubricating layer thickness as a result of the balance between normal load and viscous force. For each tested liquid it succeeds in collapsing friction measurements onto the same curve. The friction analysis for both lubrication theory and experiments then reveals that shear thinning mainly changes the layer thickness, which is the main determinant of the friction coefficient.

DOI: [10.1103/PhysRevApplied.19.014056](https://doi.org/10.1103/PhysRevApplied.19.014056)

I. INTRODUCTION

To understand the physics behind lubrication there are many parameters to be considered. Because of the importance of friction and lubrication, over the years researchers have tried to find, both experimentally and theoretically, relations between the various parameters that play a role in lubrication. In particular, predicting the lubricating layer thickness and friction coefficient is important as knowledge about these two parameters is required, for example, to reduce energy loss due to frictional dissipation or to extend the lifetime of mechanical components.

In the early 1900s, well-documented lubrication experiments were performed, and the phenomenology established back then still stands today [1,2]. It was found that there are three different regimes for lubricated friction: the boundary and mixed regimes in which surface properties of the solids play an important role, and the hydrodynamic regime in which the layer thickness is so large that the physics is fully determined by the hydrodynamics of the fluid in the contact. The point of minimal friction is found in the transition between mixed and hydrodynamic regimes.

Since then, much more work has been done, both from a theoretical viewpoint and experimentally. A well-accepted conclusion from theory is that, for the lubrication of soft deformable surfaces, an extra regime, the elasto-hydrodynamic regime, should be introduced between the mixed

and hydrodynamic regimes to account for the interplay between surface deformation and hydrodynamic pressure [3–5]. For non-Newtonian liquids many models have been proposed to account for variable viscosity [6–9], yield stress [10], normal stresses [11,12], and other complex flow properties of the lubricating fluids [6,9,13]. Even more advanced is the combination of deformable surfaces and non-Newtonian properties [14]. It has, however, proven difficult to quantitatively test non-Newtonian fluid models in a practical experimental setup, because they typically consist of a lengthy mathematical calculation involving many intertwined parameters, which gives little room for systematic and independent variation of the different fluid properties in experiments. A Carreau-Yasuda shear-thinning-fluid model, for example, already has four parameters, so three extra parameters compared with a Newtonian liquid [15,16]. These parameters strongly and simultaneously vary with, for instance, the polymer concentration, so that determining the effect and relevance of each of these parameters on lubrication is difficult.

Recently, a quantitative description was developed for the lubrication of Newtonian fluids that successfully predicts friction [17]. We extend this model here to non-Newtonian fluids. In Ref. [17] a model was proposed regarding the lubricating layer thickness and friction coefficient in a simple lubrication experiment involving hard-on-hard surfaces with a Newtonian liquid in the hydrodynamic regime. In practice, this model is of limited use as many realistic situations involve lubrication additives that lead to shear thinning and elasticity, which cause very

*d.bonn@uva.nl

different lubricating behavior. Here we describe a model for lubrication experiments involving such fluids, which is of high relevance for understanding, for example, the sensory attributes of food and hygiene products, which typically exhibit complex properties. We measure the lubricating properties of aqueous polymer solutions exhibiting either strong shear thinning or large elastic effects, and find that the shear thinning is by far the dominant effect accounting for the differences with Newtonian lubrication. We therefore develop a model along the lines of Ref. [17], in which we capture the viscosity in a power-law model,

$$\eta(\dot{\gamma}) = m\dot{\gamma}^{n-1}, \quad (1)$$

with m and n the fluid parameters and $\dot{\gamma}$ the (absolute) shear rate [15]. Compared with Newtonian liquids, this effectively adds only one parameter, as the Newtonian viscosity η is now replaced by the pair (m, n) , where m is a measure for the viscosity increase compared with the solvent, and n quantifies the degree of shear thinning. We produce non-Newtonian fluids that are well described by the power-law model over the relevant range of shear rates, and show that the non-Newtonian friction model, while relatively simple, enables us to describe relevant experimental situations. This allows us then to develop an understanding of the effect of shear-thinning lubricants on the shape of the Stribeck curve that gives the friction as a function of the ratio of the squeezing and lift forces.

II. METHODS

The experimental setup consists of a disk (of radius $R_s = 1.95$ cm) with a curved bottom (with radius of curvature $R = 1.00$ m) being pulled by an arm attached to a rheometer along a circular glass track covered in lubricant, see Figs. 1(a) and 1(b). The rheometer measures the torque required to pull the disk with constant velocity and hence the total friction on the disk can be retrieved. Induction sensors just underneath the glass track allow for layer thickness measurements with about $5\text{-}\mu\text{m}$ precision each time the disk slides over one of them. Additional mass can be added centrally on top of the disk to test a variety of different loads. For a more detailed description of the setup, refer to Ref. [17].

The accuracy of $5\text{ }\mu\text{m}$ is obtained by repeatedly performing the calibration described in Ref. [17]. All calibration curves formed this way are identical within a margin of $5\text{ }\mu\text{m}$. This is also found during the dry measurements that are performed before any measurements with lubricant take place. For a layer thickness of “zero” (in the absence of lubricant), the sensor values always agree with each other within this $5\text{ }\mu\text{m}$ error. The error is likely caused by the path, position, and tilt of the disk fluctuating on the micrometer scale when repeatedly sliding over the sensors, in both dry and lubricated circumstances.

Nine liquids are tested: four concentrations of poly(ethylene oxide) (PEO) with chain length 4 000 000 (ranging from 2.5 g/l to 10.0 g/l, labeled as “4M”), one concentration of PEO with chain length 2 000 000 (10.0 g/l, labeled as “2M”), one concentration of xanthan gum (5 g/l, from *Xanthomonas campestris*), one shear-thickening concentration made with cornstarch, and, as a reference Newtonian fluid, we use two types of silicon oil with constant viscosities of 53.5 mPa s and 104 mPa s, as in Ref. [17]. All polymers are from Sigma Aldrich and diluted in demineralized water. For the shear-thinning liquids, the flow curves are measured with a rheometer following standard rheological procedures [18] and are shown in Figs. 1(c) and 1(d). A power-law fit is made for the range $\dot{\gamma} = [30, 600]\text{ s}^{-1}$, as a quick order-of-magnitude calculation reveals that this covers the expected shear rates in our experimental setup. The resulting parameters m and n are listed in Figs. 1(c) and 1(d). Both the rheological experiment and the sliding experiment are performed at a constant temperature of 19°C .

The reason for choosing these specific polymers is the following. The long, flexible chains of PEO polymers are known for giving rise to large elastic stresses, evident as a large first normal stress coefficient [15]. The way the polysaccharide chains of the xanthan gum are assembled, on the other hand, make these polymers stiff; macroscopically, this is evident from the strong shear thinning with almost negligible elastic stresses [19]. The measurement by a rheometer [see inset in Fig. 1(d)] confirms this: the elastic effects are very pronounced for the flexible PEO, and show up as a large normal stress. This is interesting from a lubrication point of view since, in principle, such normal stresses can provide an extra lift force, thickening the lubrication layer. In line with the idea that the elasticity is due to the stretching of the individual polymer chains in the flow, we find that the PEO 10 g/l (2M) solution is less viscoelastic than PEO 10 g/l (4M) due to the polymers’ shorter chain length, but still exhibits significantly more normal stress than the xanthan gum at high shear rates. As the polymer solutions have such different viscoelastic properties, but similar shear-thinning viscosity profiles, they allow us to also disentangle the effects of normal stresses.

III. RESULTS

Figure 2 shows the results of the layer thickness measurements. The surprise is that, despite the large difference in elastic effects among the tested liquids, no significant difference in behavior is observed in the measured layer thicknesses. If viscoelasticity were to have any impact on the generated layer thickness, this should become apparent in the data for small layer thickness and high velocities, for which the high shear rate causes the normal stress to become important. However, Fig. 2 shows in

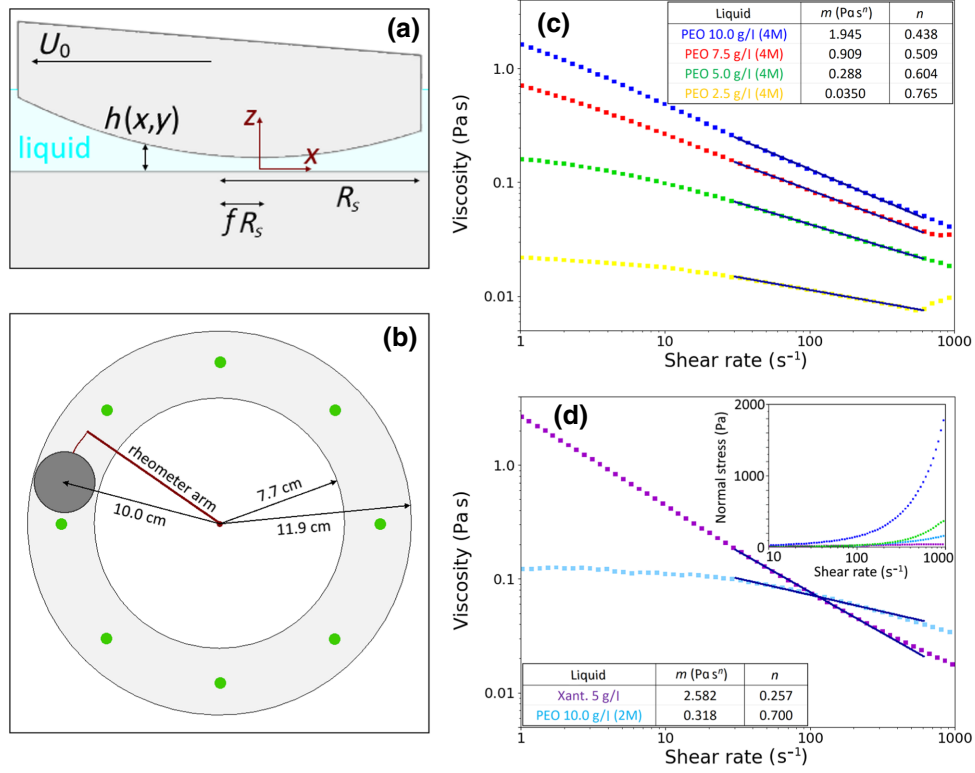


FIG. 1. (a),(b) Schematics of the side view (a) and top view (b) of our setup, identical to Ref. [17]. The disk is pulled with velocity U_0 by a rheometer arm over a glass track covered in lubricant. Eight induction sensors just underneath the glass allow for the measurement of the central layer thickness h_0 , i.e., the narrowest part of the gap in (a). The disk is slightly tilted in such a way that this point is shifted by an amount $f R_s$ in the x direction. (c),(d) Flow curves of the four concentrations PEO 4M (c) and of the PEO 2M and xanthan gum solutions (d) as measured by a rheometer. The dark blue lines show power-law fits $\eta(\dot{\gamma}) = m\dot{\gamma}^{n-1}$ for shear rates $\dot{\gamma}$ from 30 to 600 s^{-1} . The corresponding values of m and n are shown in the legends. Inset in (d) shows the normal stress for the PEO 10 g/l (4M), PEO 5 g/l (4M), PEO 10 g/l (2M), and xanthan gum concentrations measured by a rheometer; the color code is that of the main figures (c),(d).

fact the opposite effect. The blue data points in Fig. 2(a) represent the measurement where the highest normal stress is expected, but the layer thickness exhibits qualitatively the same behavior as all other measurements shown, such as the red data points in Fig. 2(c), for which the lowest normal stress is expected. For all measurements, the layer thickness increases with velocity in a similar fashion. Although PEO 10 g/l (4M) can sustain a slightly higher load than the other two liquids, this happens because this solution is much more viscous in the relevant range of shear rates than the other two liquids, and this is not due to the viscoelastic properties. We quantify these remarks in the following.

IV. THEORY

For a Newtonian liquid, the dependence of the friction coefficient on the experimental parameters is usually described as a Stribeck curve, which gives the friction as a function of the Hersey number, a dimensionless group that compares viscous to normal forces. The theoretical description of a Newtonian liquid lubricating our disk [17]

can be modified by imposing the viscosity given in Eq. (1) in the lubrication approximation at the start of the calculation. Thereafter, the calculation follows the same steps as for a Newtonian liquid, although the presence of the fractional power n in the expressions makes the calculation more cumbersome. This is, firstly, because the velocity profile of a power-law liquid between two walls can only be written in an implicit form [20] and, secondly, because commercial differential equation solvers (like *Mathematica*) are typically not optimized to deal with differentials raised to a fractional power. Therefore, we use a custom-made finite-element approach to solve the pressure profile underneath the disk (see Appendix; see [21] for more details). Viscoelasticity is not included in the model.

The following equations for lift and friction underneath a disk lubricated by a power-law liquid are obtained by substituting Eq. (1) into the lubrication equations,

$$F_N = 2^{1+n} \left(\frac{1}{n} + 1 \right)^n \frac{m U_0^n R^{1+n}}{R_s^{2n-1}} \Lambda_n(\tilde{R}_s), \quad (2)$$

$$F_w = 2^n m U_0^n R_s^{2-2n} R^n K_n(\tilde{R}_s), \quad (3)$$

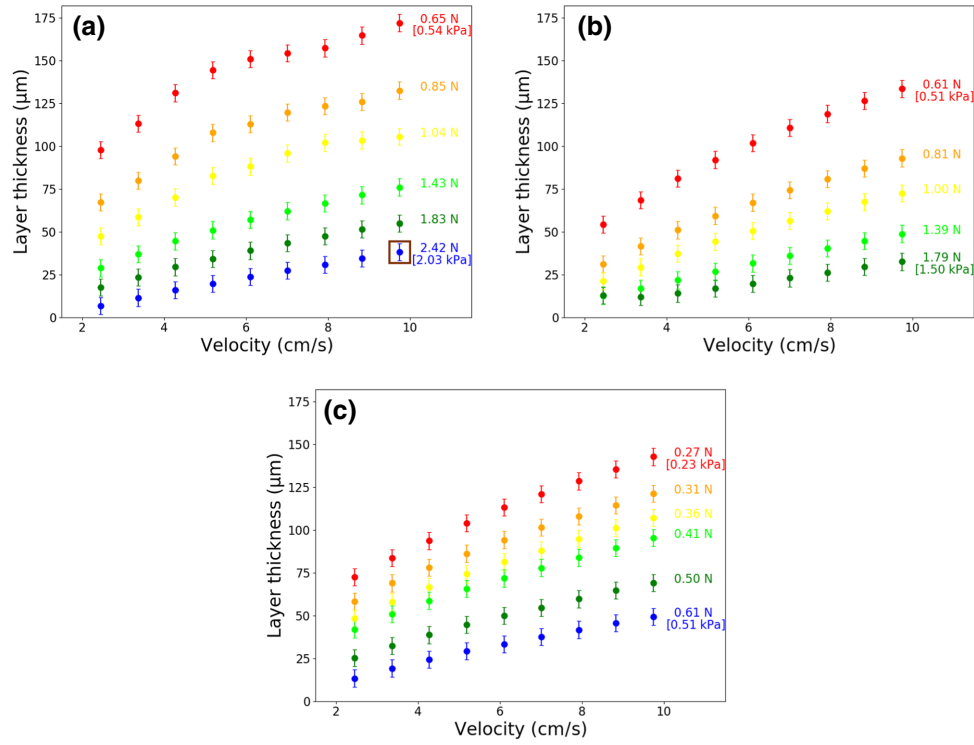


FIG. 2. Layer thickness results for (a) PEO 10 g/l (4M), (b) PEO 10 g/l (2M), and (c) xanthan gum 5 g/l. The forces next to the data denote the load on the disk and the error bars display the 5- μm measurement error. The stresses in square brackets denote the mean normal stress present underneath the disk. Despite their difference in viscoelasticity, all three liquids show similar response on layer thickness when velocity and load is varied. For the point marked with a brown box in (a) the lift due to normal stresses is estimated in the main text.

with R the radius of curvature underneath the disk, R_s the radius of the disk, U_0 the sliding velocity, and (m, n) the power-law parameters. $\Lambda_n(\tilde{R}_s)$ and $K_n(\tilde{R}_s)$ are dimensionless functions determined by the numerical solution of the pressure profile. The liquid layer thickness h_0 manifests itself in the equations through the dimensionless parameter $\tilde{R}_s = R_s/\sqrt{2Rh_0}$. Inverting Eq. (2) therefore yields a solution for the layer thickness as a function of macroscopic parameters. For Newtonian liquids, the ratio of the viscous (lift) and normal (squeezing) forces are given by the Hersey number. A dimensionless collection of parameters is found from these considerations that can be defined as the Hersey number Hr for shear-thinning fluids,

$$h_0 = \frac{R_s^2}{2R} \left(\Lambda_n^{-1} \left(\frac{1}{2^{1+n}((1/n) + 1)^n \text{Hr}} \right) \right)^{-2}, \quad (4)$$

$$\text{Hr} = \frac{mU_0^n R^{1+n}}{F_N R_s^{2n-1}}. \quad (5)$$

By substituting the layer thickness Eq. (4) into Eq. (3) an expression for the friction coefficient is found,

$$\mu \equiv \frac{F_w}{F_N} = 2^n \frac{R_s}{R} \text{Hr} K_n \left(\Lambda_n^{-1} \left(\frac{1}{2^{1+n}((1/n) + 1)^n \text{Hr}} \right) \right). \quad (6)$$

The functions Λ_n and K_n depend on the power-law index n , so instead of a single Stribeck curve of friction coefficient versus the dimensionless Hersey number, a collection of Stribeck curves is found for various values of n , as plotted in Fig. 3.

The definition of Hersey number in Eq. (5) and the definitions of Λ_n and K_n are somewhat arbitrary, as any multiplication with a constant depending on n will result in an equally acceptable definition. An obvious choice is to include the factor $2^{1+n}((1/n) + 1)^n$ into the definition of the Hersey number as well, which has the benefit of changing the curves in Fig. 3 in such a way that they cover approximately the same range of Hersey numbers, making them easier to compare. However, the power-law index always remains present in the dimensionless form of the equations, so it is impossible to exactly collapse all the curves shown in Fig. 3(a) onto a single “universal” Stribeck curve as can be done for Newtonian fluids [17]. The concept of Hersey number is typically used as a simple means of comparing data from several measurements, so the simplest form without any extra constants presented in Eq. (5) is probably the most logical from a practical point of view.

It is important to note that because of this freedom of choice about how the Hersey number depends on n , Fig. 3(a) does not allow for a proper comparison of friction

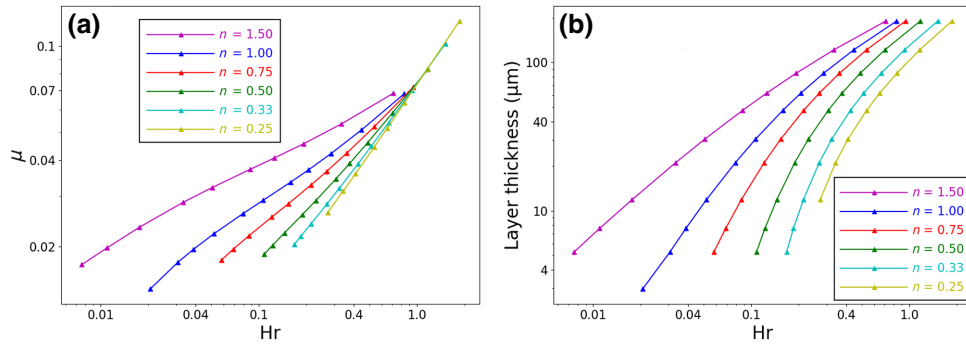


FIG. 3. (a) Modeled Stribeck curves (representing the relation between Hersey number and friction coefficient) for several values of n as calculated by Eq. (6). (b) Lubricating layer thickness as function of Hersey number as calculated by Eq. (4). For both plots, the Hersey number as defined in Eq. (5) is used and the values $R_s = 1.95$ cm and $R = 1.00$ m are used to reflect the experimental situation. Data points represent values calculated by the finite-element implementation, and are connected by a spline for visual guidance.

between liquids with different power-law indices. For our choice of Hr , it may appear that a lower friction is obtained for lower n , but Fig. 3(b) shows that for this Hr the layer thickness also drains more quickly for lower n . The Hersey number for which the transition between mixed and hydrodynamic lubrication takes place depends, therefore, on n , which should be kept in mind when considering Fig. 3(a). Though no shear-thickening liquids are tested experimentally here, it is worth noting that the model also yields results for $n > 1$, as shown by the purple $n = 1.50$ lines in Fig. 3.

One of the strengths of our model is that no complicated description of the flow curve is required, in contrast with other suggested models. The only fluid parameter needed is a power-law approximation to the part of the flow curve that falls in the range of the expected shear rate within the lubricated contact. Other knowledge of the flow curve is not needed. This task is relatively easy compared with implementing a more difficult fluid model and it should capture all first-order effects due to the nonconstant liquid viscosity. From a practical point of view, a deeper understanding of the higher-order effects may not be needed.

V. COMPARISON OF THEORY AND EXPERIMENTS

Figure 4 shows the comparison between the theory described previously and our measurements of the lubricating layer thickness on the different liquids. It is found that for all measurements on non-Newtonian liquids, the predicted layer thickness is somewhat lower than the measured one; for Newtonian liquids the model and experiments agree. We do, however, find that the model describes the experiments provided we scale the model outcomes by a constant C of order unity. For three of the tested liquids the results of this procedure are shown in Fig. 4.

The constant C required to collapse model and experiments is obtained by minimizing the rms difference between data and fit for each of the tested liquids, and is shown in the table [Fig. 4(d)].

Because the hydrodynamic description works well for Newtonian liquids, and because the non-Newtonian approach follows exactly the same steps, it is likely that the deviation has a physical origin rather than a mathematical one. The shear-thinning liquids lubricating more than theorized may be an artefact of the limitations of the power-law model. Even though the power-law covers the majority of the expected shear-rate range underneath the disk, it generally underestimates the viscosity at shear rates higher than 600 s^{-1} . Locally, shear rates higher than this value are reached underneath the disk. Moreover, the flow profile in the rheometer experiment (a simple shear flow) is different from the flow profile underneath the disk, and with nonconstant viscosity it must be kept in mind that the stresses in the fluid might not follow the same relation with respect to shear rate when the configuration is altered. This is especially true for configurations for which the shear rate tensor $\dot{\gamma}$ has more than one nonzero element (which is true for the lubricated disk, and not for the rheometer). In fact, the theoretical description contains the hidden assumption that the fluid displays identical viscous behavior in both the rheometer and the sliding experiment. In this context, we might say that C being close to unity, but not being exactly unity, serves as proof that this assumption is reasonable, but not perfect.

A similar kind of analysis can be performed on the friction data. If for each data point the corresponding Hersey number and friction coefficient are calculated, all measurements collapse onto a single curve for each separate liquid, see Fig. 5 and Fig. 9 in the Appendix and Fig. 9 in [21]. The Hersey number for power-law fluids, as given in Eq. (5), therefore satisfies one of the desired properties of such a dimensionless number, namely that

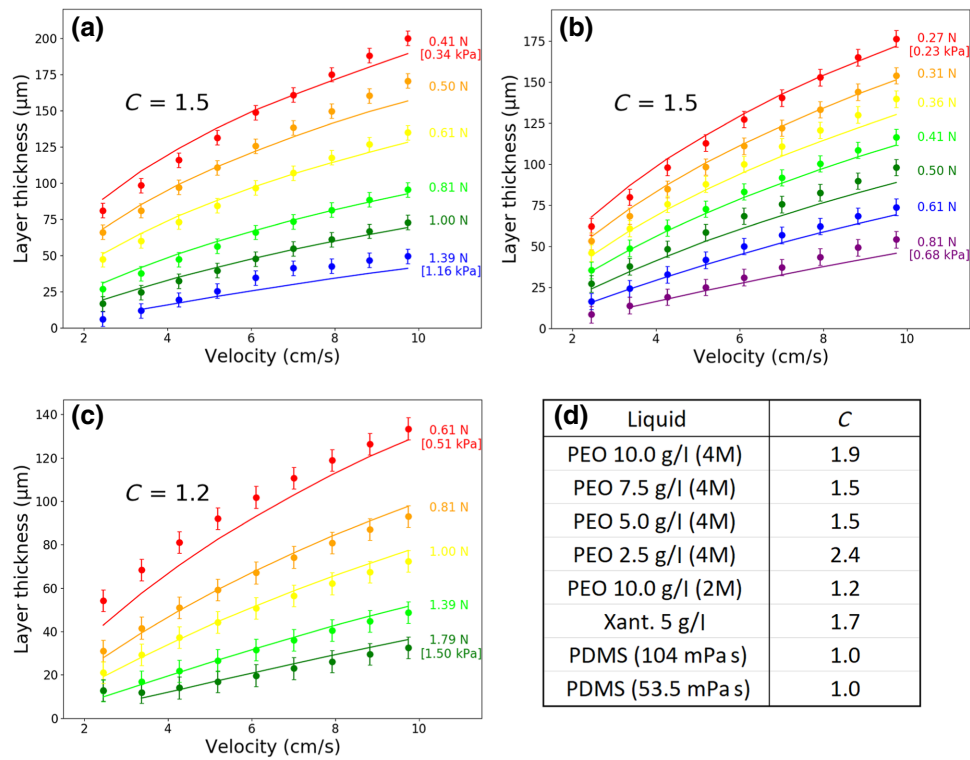


FIG. 4. (a)–(c) Layer thickness as determined by experiments (symbols) and model outcomes multiplied by constant C (solid lines) for (a) PEO 7.5 g/l (4M), (b) PEO 5.0 g/l (4M), and (c) PEO 10.0 g/l (2M). The forces next to the data denote the load on the disk. The stresses in square brackets denote the mean normal stress present underneath the disk. (d) Fitted values of C for all tested liquids.

it relates different measurements within the same physical framework. It is already anticipated that different liquids have different Stribeck curves, since they all have different power-law indices n .

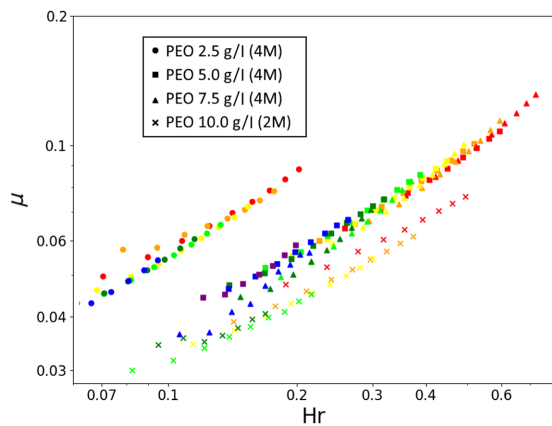


FIG. 5. Friction coefficient μ as a function of Hersey number as defined in Eq. (5), for PEO 2.5 g/l (4M), PEO 5.0 g/l (4M), PEO 7.5 g/l (4M), and PEO 10.0 g/l (2M). (A plot of the other liquids can be found in Fig. 9 in [21] and in the Appendix.) Colors represent series of measurements with different normal force, and are equivalent to the colors used in Fig. 4. For each liquid all data points fall onto a single curve, highlighting the usefulness of the Hersey number as defined in Eq. (5).

To investigate the effect of shear thickening on the lubrication properties of a liquid, the same sliding experiment is performed with a cornstarch-water mixture. The creation of a suitable shear-thickening liquid is trickier than for the polymer concentrations, and generally the flow curve of such a liquid is more complicated [see Fig. 6(a)]. For the cornstarch solution, sedimentation of the particles over time changes the rheology of the fluid and, therefore, the quality of the measurement degrades quickly over time. Despite these difficulties, the cornstarch solution clearly displays shear-thickening properties under the rheometer. Within the relevant shear-rate range $\dot{\gamma} = [30, 600] \text{ s}^{-1}$ a power-law index of $n = 1.52$ is retrieved.

For the sliding experiment, the expected trend is observed for the shear-thickening solution compared with a Newtonian and a shear-thinning liquid [see Fig. 6(b)]. The layer thickness grows more strongly with velocity for the cornstarch solution than for the other two displayed examples as a result of the liquid getting thicker when a higher shear rate is applied. For Newtonian and shear-thinning liquids, the layer thickness grows sublinearly with velocity, whereas for this particular cornstarch solution, a superlinear trend is found. The layer thickness does not go to zero for low velocity, but instead stays at $100 \mu\text{m}$, which might be a result of either particle sedimentation or the liquid's yield stress. However,

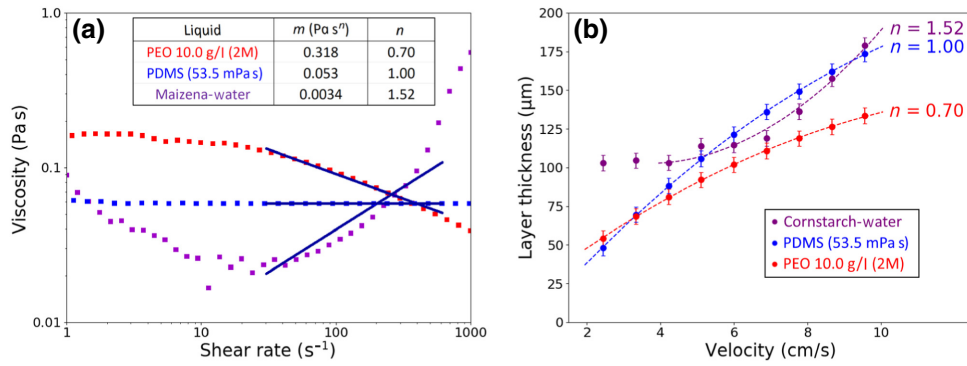


FIG. 6. (a) The flow curve of a shear-thinning liquid [PEO 10.0 g/l (2M)], a Newtonian liquid [polydimethylsiloxane (PDMS) oil], and a shear-thickening liquid (cornstarch in water) as measured by a rheometer. The dark blue lines show power-law fits for shear rates between 30 and 600 s^{-1} , of which the corresponding parameters m and n are displayed in the legend. (b) Layer thickness as a function of velocity as measured in the sliding setup for the same three liquids. The dashed lines visualize the trend. For the shear-thinning and Newtonian liquid, this trend is sublinear, whereas the shear-thickening liquid displays a superlinear trend. The normal forces applied on the disk are 0.27 N for the PEO, 0.41 N for the oil, and 0.23 N for the cornstarch.

the superlinear trend in Fig. 6(b) is rather strong, even when a large uncertainty is considered on the left-most data points.

VI. DISCUSSION

The first conclusion from the overlap between the xanthan and PEO data is that there is no extra lift force generated in our experiments due to the normal stresses that are present for PEO and almost absent for xanthan. If we assume the relation between normal stress and shear rate as found in the rheometer holds underneath the disk, an estimate for the predicted lift due to elasticity can be found in the following manner. Via the measured central layer thickness, the shear rate underneath the disk can be approximated as $\dot{\gamma} \approx U_0/h(r)$, with $h(r)$ the general layer thickness underneath the disk. The lift due to elasticity can then be found by integration of the normal stress over the entire disk, $F_{N,elastic} = \int_{Disk} N_1(\dot{\gamma})dA$, with the relation $N_1(\dot{\gamma})$ measured by the rheometer [see the inset of Fig. 1(d)]. Performing these operations for the marked point in Fig. 2(a) yields a value of 2.13 N, which is of the same order of magnitude as the 2.42 N of normal force applied for this specific experiment. Therefore, this calculation suggests that elasticity *does* play an important role for some of our measurements, in contrast with our experimental findings. It must be noted, however, that the initial assumption is most likely incorrect. The flow profile underneath a moving curved disk is different from the simple shear flow between two plates of a rheometer and it is not obvious how normal stress measured in a rheometer translates to stresses present in a lubricated contact. For an upper-convected Maxwell model the elasticity has been shown to not make a large difference, and in general it does not contribute to an extra lift force depending on the exact

details of the geometry [12]. A simpler viewpoint is to take a second-order fluid model with a constant viscosity and normal stress coefficient for which exact formulas for lift generation exist [11,22]. These formulas do predict a positive contribution to the lift as a result of viscoelasticity, as we anticipate in the introduction. The implementation of this model is complicated, however, since real liquids typically display neither constant viscosity nor a constant normal stress coefficient, as is also the case for the liquids used here. In our experiments, no obvious difference between the most and least viscoelastic liquid is found; thus, we conclude that, within the range of viscosities and normal stresses that our setup allows us to test, any viscoelastic effects are irrelevant to the lubrication process and an analysis based solely on shear-thinning properties suffices.

The second question is, then, what the effect of polymer addition is. Increasing the polymer concentration in a solution increases the viscosity of the liquid, but makes the shear-thinning properties more prominent (m increases whilst n decreases), as shown in Fig. 1(c). The increase in viscosity means that a contact which is not fully lubricated can shift into the hydrodynamic lubrication regime by adding polymers to thicken that liquid, resulting in a lower friction. The transition happens when the layer thickness is large enough to neglect surface properties, so the amount of polymer needed to reach the lubrication regime should be determined by Eq. (4).

Within the lubrication regime, a higher friction viscosity means it is more difficult to squeeze the liquid out of the contact, but also leads to a higher resistance to making the liquid in the contact flow. This trade-off is understood for Newtonian fluids, where the friction coefficient varies sublinearly with the Hersey number, and hence a viscosity that is twice as high leads to friction that is less

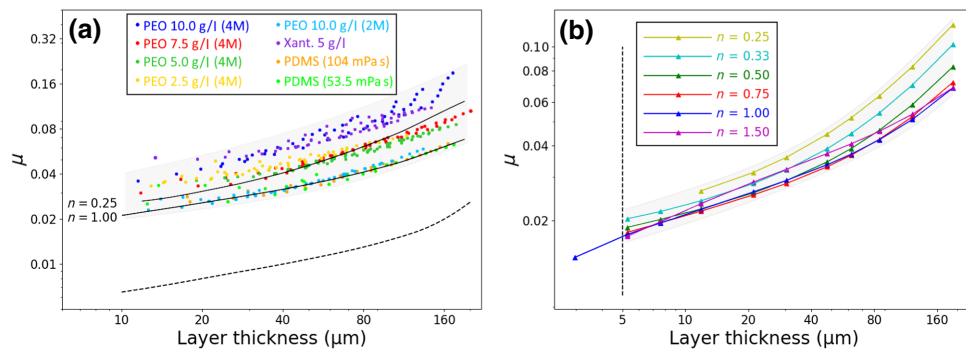


FIG. 7. (a) Experimental friction coefficient μ as function of central layer thickness. The values of the dashed line have been subtracted for all data points to compensate for noise friction, as further explained in the text. Two theoretical curves ($n = 0.25$ and $n = 1.00$) coming from the model are plotted for the sake of comparison. The data points of the experiments with shear-thinning fluids lie above those of the Newtonian fluids, which is in agreement with the prediction of the model. (b) Model predictions of the friction coefficient as a function of layer thickness for several values of n . The shaded areas in both figures display the narrow range that all results fall into. The values $R_s = 1.95$ cm and $R = 1.00$ m, representing the experimental setup, are used in Eqs. (4) and (6) to obtain the model results.

than 2 times higher [17]. For shear-thinning fluids, the comparison is more subtle. One could compare a shear-thinning polymer solution with a hypothetical Newtonian liquid with viscosity equal to the zero-shear viscosity of the liquid. The zero-shear viscosity is, in this case, an over-estimation of the actual viscosity for the relevant range of shear rates reached within the contact. Therefore, the shear-thinning fluid has a lower Hersey number and yields a lower friction than its hypothetical Newtonian counterpart, as long as the liquid is thick enough to be in the hydrodynamic lubrication regime.

However, in reality, the shear-thinning lubricant is relatively thick near the inlet and outlet of the contact, whereas it is relatively thin centrally in the contact, where the shear rate is highest. Having a thin liquid in the middle yields a lower generated lift and hence smaller layer thickness, but meanwhile the friction also reduces by having a thin liquid, according to Eqs. (2) and (3). One could therefore wonder whether the net result of these two counteracting effects could lower the point of minimal friction in a Stribeck curve for a liquid with $n < 1$. To determine the effect of shear-thinning properties on the point of minimal friction, plotting the friction as a function of a Hersey number, such as in Fig. 5, is not helpful since different liquids have different Stribeck-like curves. However, because Hersey number and layer thickness are related one-to-one with each other by Eq. (4), and the Hersey number and friction coefficient are related one-to-one by Eq. (6), it is possible to plot a different type of Stribeck curve with layer thickness and friction coefficient on the x and y axes, respectively. Plotting the branches of Stribeck curves as a function of layer thickness is a good way to compare their points of minimum friction.

The results are shown in Figs. 7(a) (experiment) and 7(b) (model). The latter shows that, when plotted as

a function of layer thickness, the friction coefficients are very similar, and lie within a narrow band. For a quantitative comparison with experiments, we have to account for the fact that in our experiments there is also a contribution from the sides rather than the bottom of the disk. In Ref. [17] we showed that a simple compensation makes theory and experiments agree for the tested silicon oils. In Fig. 7(a), we subtract the values corresponding to the dashed line for all the data discussed previously, in order to again find that the Newtonian liquids collapse with the predicted friction coefficient. The power-law fluids appear to fall within a narrow band predicted by the theory. The small differences are systematic, and show that the friction is higher for the non-Newtonian liquids, and becomes more so when the shear thinning increases: we find that the most shear-thinning liquids tested [PEO 10.0 g/l (4M) and xanthan 5.0 g/l with $n = 0.438$ and $n = 0.257$, respectively] give rise to the highest friction curves, also validating the predictions from our model.

Could the polymer then help very thin films to stay in the lubricated regime, instead of transiting to the mixed lubrication regime? In our setup we expect the transition between hydrodynamic and mixed regimes to occur at a layer thickness under $5 \mu\text{m}$ [17], because the roughness of the disk is of order $1 \mu\text{m}$. It is clear, however, in Fig. 7(b) that at $h_0 = 5 \mu\text{m}$ shear-thinning properties cause the friction to be higher than for a Newtonian liquid. In other words, shear-thinning properties do *not* help when trying to reduce energy losses in a lubricated contact. For any contact lubricated by a shear-thinning lubricant, there will always be a Newtonian liquid that has a lower point of minimal friction in its Stribeck curve, within the scope of effects considered in this article.

Judging from the line $n = 1.50$ in Fig. 7(b), it might be the case that shear-thickening fluids can reduce the

minimum friction, although we have no experimental results to support this hypothesis. In a broader view, this result might also be interesting for liquids exhibiting pressure-viscosity effects, as these liquids have a higher viscosity in the region of high shear rate too, mimicking a shear-thickening effect.

The small difference in friction coefficients when plotted as a function of layer thickness is perhaps useful for predicting friction in other systems. If one would like to understand the lubrication properties of a complex liquid of which the flow curve is known, there are two possible approaches. In both cases, one would start by estimating the generated layer thickness either using Eq. (4) or the equivalent Fig. 3(b). One can subsequently determine the friction using Eq. (6) or the equivalent Fig. 3(a). The other option would be to use Fig. 7(b) to predict the friction. The latter method has the added benefit that the liquid might as well be considered Newtonian from that point forward due to the weak dependence on n . This also means that comparing the lubrication properties of multiple different complex liquids simplifies down to the comparison of only their generated layer thicknesses.

It is not obvious yet whether the conclusion that shear-thinning fluids are not useful for lowering the point of minimum friction in the Stribeck curve holds if the contact is deformable or if a rolling contact is used. Rolling and sliding friction are similar in lift generation, but differ by the absence of the so-called “Couette contribution” to the shear stress in the case of a rolling contact [23]. For shear-thinning liquids, the Couette term tends to be larger than for Newtonian liquids at the edge of the disk, so it is imaginable that the removal of this term will result in shear-thinning liquids being favorable when it comes to friction reduction.

The microscopic gap between two lubricated deformable surfaces takes approximately the shape of two parallel walls in which the lubricant reaches its highest shear rate [24]. It can be hypothesized that in this area a shear-thinning liquid yields less friction than a Newtonian liquid, as the liquid gets “thin” in this region of high shear rate. To verify this hypothesis though, lift generation with shear-thinning fluids in a deformable gap must also be understood. This requires a more thorough analysis of the interplay between all the parameters involved.

The results predicted by the model are in principle not limited to the range of parameters our setup allows us to test. One criterion is that the generated layer thickness must be large enough to validate a fully hydrodynamic description of the liquid within the contact. Surface effects start playing a role if the layer thickness reaches the same order of magnitude as the surface roughness. Similarly, if the layer thickness has the same order of magnitude as the particles that make up the fluid, for example, the droplets in an emulsion, the flow curve as measured by a rheometer will not describe the fluid’s behavior in the gap correctly.

For a large enough layer thickness, the main limitation of the model is most likely the precision with which a power law can describe the viscous properties of the liquid over a large range of shear rates. The power law is a very simplified way to define a fluid’s viscous behavior with only two parameters m and n , and our work shows that these two parameters are sufficient to give a good approximation of the lubricating behavior of a liquid. However, these two parameters by themselves can never perfectly describe the complex molecular interactions that occur in nontrivial flow profiles.

Another criterion is that the forces are low enough to guarantee the surfaces will not deform, otherwise an elastohydrodynamic description is required. Whether viscoelastic stresses remain unimportant in a more extreme situation with higher velocity and higher force is something that remains to be investigated more deeply.

VII. CONCLUSION

To conclude, we present a simple model describing the process of lubrication with shear-thinning lubricants. Viscoelastic properties of the lubricant do not have to be taken into account, as it is shown that they play no role in the generation of the lubricating layer, at least within the range of parameters tested experimentally here. Although the underlying numerical framework of the model is more complex, the model maintains its practical form with a Hersey number as a central parameter. Provided we include a multiplication factor C of order unity in the model, it describes the behavior of both Newtonian and non-Newtonian fluids well. The practical form of the model might help others understand their results on several levels of complexity. The simplest application would be to use the Hersey number to create Stribeck curves for shear-thinning liquids, which could not be done before with the standard Newtonian Hersey number. A more advanced application would be to select the branch of Stribeck curve that represents a given fluid with power-law index n , and quantitatively predict the friction and layer thickness in the lubricated contact. Further extensions to the model, and in particular to the Hersey number, could include more complex fluid parameters or the effect of the deformability of the surfaces.

APPENDIX

The calculation of lift and friction forces on a disk lubricated by a shear-thinning fluid follows the same steps as for a Newtonian liquid, but is algebraically and computationally more difficult due to the fractional exponents that appear in the equations. The characteristic Reynolds equation for liquids more complex than Newtonian liquids is known in the literature [8,9]. However, due to the implicitness of the equations (e.g., the velocity profile depends on viscosity, which in turn is a function of shear rate,

and hence velocity) we start our derivation from basic hydrodynamic equations.

For a small layer thickness ($h_0 \ll R_s$) the Navier-Stokes equations reduce to the lubrication approximation [25],

$$\frac{\partial p}{\partial x} = \frac{\partial \tau_{xz}}{\partial z}, \quad (\text{A1a})$$

$$\frac{\partial p}{\partial y} = \frac{\partial \tau_{yz}}{\partial z}. \quad (\text{A1b})$$

In the case of a power-law fluid model, the shear stress is given by [15]

$$\tau_{xz} = m\dot{\gamma}^{n-1}\dot{\gamma}_{xz}, \quad (\text{A2a})$$

$$\tau_{yz} = m\dot{\gamma}^{n-1}\dot{\gamma}_{yz}, \quad (\text{A2b})$$

where the ‘‘absolute shear rate’’ is given by $\dot{\gamma} = \sqrt{\dot{\gamma}_{xz}^2 + \dot{\gamma}_{yz}^2}$. Because the disk is moving in x direction, the shear rate component $|\dot{\gamma}_{xz}|$ is naturally much larger than $|\dot{\gamma}_{yz}|$, so we can assume $\dot{\gamma} \approx |\dot{\gamma}_{xz}|$, greatly simplifying the derivation. By checking with the solution found previously [17] for a Newtonian liquid ($n = 1$) it can be found that everywhere in the relevant domain the shear rate $|\dot{\gamma}_{xz}|$ is at least 8 times larger than $|\dot{\gamma}_{yz}|$, which indeed validates the assumption.

Using $\dot{\gamma} \approx |\dot{\gamma}_{xz}|$ and writing $\dot{\gamma}_{xz} = \partial u_x / \partial z$ and $\dot{\gamma}_{yz} = \partial u_y / \partial z$ yields

$$\frac{\partial p}{\partial x} = m \frac{\partial}{\partial z} \left(\left| \frac{\partial u_x}{\partial z} \right|^{n-1} \frac{\partial u_x}{\partial z} \right), \quad (\text{A3a})$$

$$\frac{\partial p}{\partial y} = m \frac{\partial}{\partial z} \left(\left| \frac{\partial u_x}{\partial z} \right|^{n-1} \frac{\partial u_y}{\partial z} \right). \quad (\text{A3b})$$

The full hydrodynamic solution consists of finding a velocity profile \mathbf{u} that satisfies the boundary conditions $\mathbf{u}(z = 0) = 0$ and $\mathbf{u}(z = h) = U_0 \hat{\mathbf{x}}$ along with a pressure profile that reduces to zero at the boundaries of the disk. This is done in the typical manner for lubrication problems: first the velocity profile as a function of pressure is calculated. From this expression, the fluxes in the x and y directions can be found, after which the incompressibility constraint yields a differential equation for the pressure that can be solved numerically. Because u_y is coupled to u_x in Eq. (A3b), it is necessary to first calculate u_x . Dimensionless coordinates, layer thickness profile, pressure and velocity are introduced as respectively:

$$a^2 = \frac{x^2}{2Rh_0} \text{ and } b^2 = \frac{y^2}{2Rh_0} \text{ and } \tilde{z} = \frac{z}{h}; \quad (\text{A4a})$$

$$\tilde{h} \equiv \frac{h}{h_0} = 1 + a^2 + b^2; \quad (\text{A4b})$$

$$\tilde{p} \equiv \frac{p}{p_0} \text{ with } p_0 = k^n m \left(\frac{U_0}{h_0} \right)^n \sqrt{\frac{2R}{h_0}}; \quad (\text{A4c})$$

$$\tilde{u}_x \equiv \frac{u_x}{U_0} \text{ and } \tilde{u}_y \equiv \frac{u_y}{U_0}. \quad (\text{A4d})$$

In the following, it proves useful to have a parameter. Additionally, the upcoming algebraic expressions have many fractional powers and it proves useful to introduce the following notation that describes the action of raising a positive or negative number to a fractional power whilst maintaining its sign: $x^{*p} \equiv \text{sign}(x)|x|^p$.

An explicit equation for u_x cannot be given for a shear-thinning fluid in Couette-Poiseuille flow. A thorough investigation of this type of flow can be found in Ref. [20]. We follow an equivalent approach, with slightly different notation, to find a velocity profile that satisfies Eq. (A3a) and the boundary conditions

$$\tilde{u}_x = \beta \left(|L_m - \tilde{z}|^k - |L_m|^k \right) \text{ with } \beta \equiv \tilde{h}^k \left(\frac{\partial \tilde{p}}{\partial a} \right)^{*(1/n)}. \quad (\text{A5})$$

The extra parameter L_m can be calculated through the injective, implicit relation

$$\frac{1}{\beta} = |L_m - 1|^{(1/n)+1} - |L_m|^{(1/n)+1}. \quad (\text{A6})$$

Equation (A5) can be substituted into the dimensionless equivalent of Eq. (A3b), after which \tilde{u}_y can be solved by integrating twice and taking into consideration the boundary conditions. This yields

$$\begin{aligned} \tilde{u}_y &= \alpha (C_1 L_m^{*(1/n)} - (L_m - \tilde{z})^{*(1/n)} (C_1 - \tilde{z})) \text{ with } \alpha \\ &\equiv \tilde{h}^k \left| \frac{\partial \tilde{p}}{\partial a} \right|^{(1/n)-1} \frac{\partial \tilde{p}}{\partial b}, \end{aligned} \quad (\text{A7})$$

where C_1 is an integration constant with value $C_1 = (L_m - 1)^{*(1/n)} / ((L_m - 1)^{*(1/n)} - L_m^{*(1/n)})$, which follows from the inferred the boundary conditions.

The dimensionless fluxes in the x and y directions are then calculated to be

$$\begin{aligned} \tilde{q}_x &= \tilde{h} \int_0^1 \tilde{u}_x d\tilde{z} = \tilde{h} \beta \left(\frac{1}{k+1} L_m^{*k+1} \right. \\ &\quad \left. + \frac{1}{k+1} (1 - L_m)^{*k+1} - |L_m|^k \right), \end{aligned} \quad (\text{A8a})$$

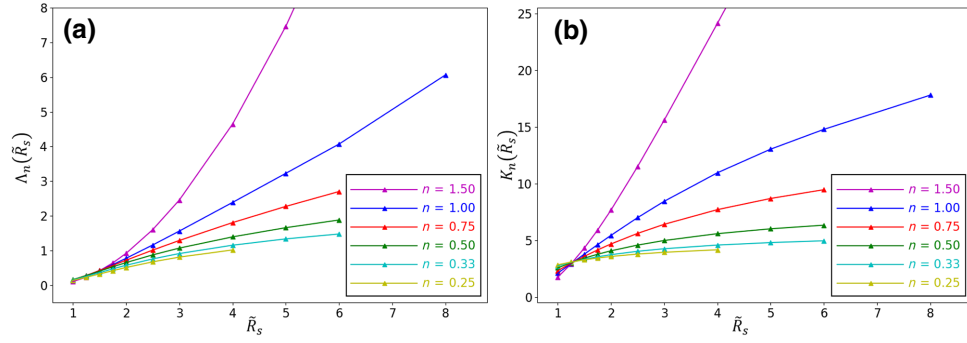


FIG. 8. Dimensionless functions (a) $\Lambda_n(\tilde{R}_s)$ and (b) $K_n(\tilde{R}_s)$ as defined in Eqs. (A13a) and (A13b) for various values of power-law index n . The points denote values calculated by the finite-element simulation and are connected by a spline curve. The blue points correspond to $n = 1$ and are equivalent to the curves in Fig. A1 in Ref. [17], which were calculated by *Mathematica*.

$$\begin{aligned} \tilde{q}_y &= \tilde{h} \int_0^1 \tilde{u}_y d\tilde{z} = \tilde{h}\alpha \left(C_1 L_m^{*(1/n)} + \frac{1}{(k+1)(k+2)} \right. \\ &\quad \times (|L_m|^k (L_m - (k+1)C_1) - |L_m - 1|^k \\ &\quad \left. (L_m - (k+1)C_1 + k)) \right). \end{aligned} \quad (\text{A8b})$$

The incompressibility constraint implies that

$$\nabla \cdot \mathbf{q} = \frac{\partial \tilde{q}_x}{\partial a} + \frac{\partial \tilde{q}_y}{\partial b} = 0. \quad (\text{A9})$$

Because the parameters β , α , and L_m all depend on pressure, this operation yields a differential equation for pressure. However, due to the fractional exponents, commercial differential equation solvers like *Mathematica* have

difficulties solving it. Therefore, a custom-made finite-element implementation is used to solve for the pressure profile. The first step consists of partial integration of the equation that is to be solved, which changes Eq. (A9), using Green's theorem, into

$$\int_{\Omega} \mathbf{q} \cdot \nabla \phi_j dA = 0. \quad (\text{A10})$$

Here Ω is the domain on which the equation is to be solved and ϕ_j are test functions that we choose to be linear tent functions with maxima at each vertex j . A total of 633 vertices are used to triangulate the grid of size \tilde{R}_s into 1176 triangles. To solve for the pressure profile, the integral in Eq. (A10) is performed for each vertex j and the pressure at each vertex is updated according to

$$p_j^{\text{new}} = p_j^{\text{old}} + S_j \int_{\Omega} \mathbf{q} \cdot \nabla \phi_j dA. \quad (\text{A11})$$

This leads to a converging scheme. The parameter S_j is introduced to manually increase the speed of convergence. (We find that updating the vertices near the boundary with lower prefactors greatly helps the rate of convergence.)

Further details of the simulation involve the tabulation of Eq. (A6) into 100 000 (β, L_m) pairs for each separate value of n , saving much calculation power as L_m values can be easily looked up. Additionally, the tilt parameter f , as defined in Ref. [17], is updated in each iteration to converge into a configuration with balancing clockwise and anticlockwise torque, according to Eq. (A9) in Ref. [17].

The lift is calculated by integration of pressure over the entire disk, where regions of $p < 0$ are excluded from the integral due to cavitation, as is typical for lubrication problems [4]. The friction force is calculated by integration of shear stress on the disk,

$$F_N = \int_D p dx dy = 2^{1+n} k^n m U_0^n R_s^{1+n} R_s^{1-2n} \Lambda_n(\tilde{R}_s), \quad (\text{A12a})$$

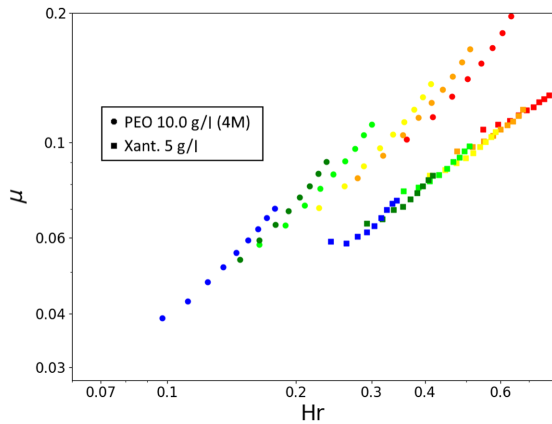


FIG. 9. Friction coefficient μ as a function of Hersey number as defined in Eq. (5), for PEO 10.0 g/l (4M) and xanthan 5 g/l (the absent liquids in Fig. 5 in the main text). Colors represent series of measurements with different normal force, and are equivalent to the colors used in Fig. 4 in the main text. For PEO 10 g/l (4M) the data points do not exactly align, which is ascribed to the large amount of drag friction the disk experiences at high velocity when ploughing through the thick yield-stress-exhibiting liquid.

$$F_w = \int_D [\tau_{xz}]_{z=h} dx dy = 2^n m U_0^n R^n R_s^{2-2n} K_n(\tilde{R}_s), \quad (\text{A12b})$$

with

$$\Lambda_n(\tilde{R}_s) = \tilde{R}_s^{2n-1} \int_D \tilde{p} da db, \quad (\text{A13a})$$

$$K_n(\tilde{R}_s) = \tilde{R}_s^{2n-2} \int_D \frac{k^n}{\tilde{h}^n} (\beta(1 - L_m)^{*(1/n)})^{*n} da db. \quad (\text{A13b})$$

The dimensionless functions $\Lambda_n(\tilde{R}_s)$ and $K_n(\tilde{R}_s)$ are plotted in Fig. 8 for several different values of n . For $n = 1.0$ our algorithm finds the same values as the *Mathematica* approach used in Ref. [17], giving confidence that the algorithm is implemented correctly.

Figure 9 shows the same type of plot as Fig. 5 in the main text, but for the two liquids that are not shown there. Also for these two liquids the data points collapse onto roughly a single curve when friction coefficient is plotted against Hersey number.

-
- [1] M. D. Hersey, The laws of lubrication of horizontal journal bearings, *J. Wash. Acad. Sci.* **4**, 542 (1914).
- [2] B. Jacobson, The Stribeck memorial lecture, *Tribol. Int.* **36**, 781 (2003).
- [3] B. J. Hamrock, S. R. Schmid, and B. O. Jacobson, *Fundamentals of fluid film lubrication* (Marcel Dekker, New York, 2004).
- [4] C. H. Venner and A. Lubrecht, *Multilevel methods in lubrication* (Elsevier, Amsterdam, 2000).
- [5] Y. Zhang, N. Biboulet, C. H. Venner, and A. A. Lubrecht, Prediction of the Stribeck curve under full-film elastohydrodynamic lubrication, *Tribol. Int.* **149**, 105569 (2020).
- [6] S. Akbarzadeh and M. M. Khonsari, Performance of spur gears considering surface roughness and shear thinning lubricant, *J. Tribol.* **130**, 021503 (2008).
- [7] Y. Xu and J. R. Stokes, Soft lubrication of model shear-thinning fluids, *Tribol. Int.* **152**, 106541 (2020).
- [8] S. Bair and M. M. Khonsari, in *World Tribology Congress III* (2005).
- [9] Y. Peiran and W. Shizhu, A generalized Reynolds equation for non-Newtonian thermal elastohydrodynamic lubrication, *J. Tribol.* **112**, 631 (1990).
- [10] C. Dorier and J. Tichy, Behavior of a Bingham-like viscous fluid in lubrication flows, *J. Nonnewton Fluid Mech.* **45**, 291 (1992).
- [11] P. Huang, Z. Li, Y. Meng, and S. Wen, Study on thin film lubrication with second-order fluid, *J. Tribol.* **124**, 547 (2002).
- [12] J. A. Tichy, non-Newtonian lubrication with the convected Maxwell model, *J. Tribol.* **118**, 344 (1996).
- [13] A. E. Cook, Some asymptotic results in hydrodynamic lubrication theory, *Appl. Math. Modelling* **9**, 72 (1985).
- [14] R. T. Lee and B. J. Hamrock, A circular non-Newtonian fluid model: Part I – used in elastohydrodynamic lubrication, *J. Tribol.* **112**, 486 (1990).
- [15] R. B. Bird, R. C. Armstrong, and O. Hassager, *Dynamics of polymeric liquids Volume 1: fluid mechanics*, 2nd ed. (Wiley, New York, 1987).
- [16] M. L. Olivares, K. Shahrivar, and J. de Vicente, Soft lubrication characteristics of microparticulated whey proteins used as fat replacers in dairy systems, *J. Food Eng.* **245**, 157 (2019).
- [17] B. Veltkamp, K. P. Velikov, C. H. Venner, and D. Bonn, Lubricated Friction and the Hersey Number, *Phys. Rev. Lett.* **126**, 044301 (2021).
- [18] T. G. Mezger, *The rheology handbook* (Vincentz Network GmbH & Co KG, Hanover, 2006).
- [19] D. Bonn and J. Meunier, Viscoelastic Free-Boundary Problems: Non-Newtonian Viscosity vs Normal Stress Effects, *Phys. Rev. Lett.* **79**, 2662 (1997).
- [20] G. Davaa, T. Shigechi, and S. Momoki, *Plane Couette-Poiseuille Flow of Power-Law Non-Newtonian Fluids, Reports of Faculty of Engineering* (Nagasaki University, Nagasaki, 2000), vol. 30, p. 29.
- [21] See Supplemental Material at <http://link.aps.org/supplemental/10.1103/PhysRevApplied.19.014056> for the implementation of a finite element algorithm to find the pressure distribution underneath the sliding disk and for two additional figures.
- [22] R. I. Tanner, *Engineering rheology* (Oxford University Press, Oxford, 2000).
- [23] M. Ankouni, N. Biboulet, and A. A. Lubrecht, Load carrying capacity and friction in starved hydrodynamically lubricated circular contacts, *J. Eng. Tribol.* **227**, 1438 (2013).
- [24] J. H. Snoeijer, J. Eggers, and C. H. Venner, Similarity theory of lubricated Hertzian contacts, *Phys. Fluids* **25**, 101705 (2013).
- [25] H. Bruus, *Theoretical microfluidics* (Oxford University Press, Oxford, 2008).